

Electrodifusion: A continuum modeling framework for biomolecular systems with realistic spatiotemporal resolution

Benzhuo Lu*

Howard Hughes Medical Institute, Center for Theoretical Biological Physics, University of California at San Diego, La Jolla, CA, 92093-0365

Yongcheng Zhou

Howard Hughes Medical Institute, Center for Theoretical Biological Physics, Department of Mathematics, University of California at San Diego, La Jolla, CA, 92093-0365

Gary A. Huber

Howard Hughes Medical Institute, University of California at San Diego, La Jolla, CA, 92093-0365

Stephen D. Bond

Department of Computer Science, University of Illinois at Urbana-Champaign, Urbana, IL, 61801

Michael J. Holst

Department of Mathematics, Center for Theoretical Biological Physics, University of California at San Diego, La Jolla, CA, 92093

J. Andrew McCammon

Howard Hughes Medical Institute, Center for Theoretical Biological Physics, Department of Chemistry and Biochemistry, Department of Pharmacology, University of California at San Diego, La Jolla, CA, 92093-0365

*Author to whom correspondence should be addressed. Fax: 1 858 534-4974. Electronic mail: blu@mccammon.ucsd.edu

Abstract

A computational framework is presented for the continuum modeling of cellular biomolecular diffusion influenced by electrostatic driving forces. This framework is developed from a combination of state-of-the-art numerical methods, geometric meshing and computer visualization tools. In particular, a hybrid of (adaptive) finite element and boundary element methods is adopted to solve the Smoluchowski equation (SE), the Poisson equation (PE), and the Poisson-Nernst-Planck equation (PNPE) in order to describe electrodiffusion processes. The finite element method is used because of its flexibility in modeling irregular geometries and complex boundary conditions. The boundary element method is used due to the convenience of treating the singularities in the source charge distribution and its accurate solution to electrostatic problems on molecular boundaries. Nonsteady-state diffusion can be studied using this framework, with the electric field computed using the densities of charged small molecules and mobile ions in the solvent. A solution for mesh generation for biomolecular systems is supplied, which is an essential component for the finite element and boundary element computations. The uncoupled Smoluchowski equation and Poisson-Boltzmann equation (PBE) are considered as special cases of the PNPE in numerical algorithm, and therefore can be solved in this framework as well. Two types of computations are reported in the results: stationary PNPE and time-dependent SE or Nernst-Planck equations (PN) solutions. A biological application of the first type is the ionic density distribution around a fragment of DNA determined by the equilibrium PNPE. The stationary PNPE with non-zero flux is also discussed for a simple model system. The second is a time-dependent diffusion process: the consumption of the neurotransmitter acetylcholine (ACh) by acetylcholinesterase (AChE), determined by the SE and a single uncoupled solution of the Poisson-Boltzmann equation. The electrostatic effects, counterion compensation, spatiotemporal distribution, and diffusion-controlled reaction kinetics are analyzed and different methods are compared.

I. INTRODUCTION

The density distribution of molecular species is fundamental in understanding and describing biophysical and biochemical processes. The concentrations of ligands (for example, substrates), receptors (enzymes), and ions regulate nearly all biomolecular and cellular activities.

Modern microscopic imaging technology (see ref. 1) enables the monitoring of physiological activity in cells with increasingly higher spatial and temporal resolution. The translocation and concentration variation of biomolecules or reagents can now be observed in real time. It has become possible to measure molecular locations and monitor subcellular signaling processes *in vivo*. Direct observations are possible for the spatially nonuniform distribution of species and the time-dependence of chemical processes. In addition, recent progress in determining the 3D structures of biomolecules (such as ion channels) or even organelles (such as synaptic vesicles) has supplied a wealth of information which greatly facilitates theoretical modeling and numerical simulation of these systems. With such information from experiments, the demand is emerging for dynamical modeling with subcellular spatiotemporal resolution. However, molecular dynamics simulations at atomic level resolution are still not tractable for such time and length scales. Therefore, we resort to continuum models due to their ability to efficiently resolve features on different space and time scales.

Variations in concentration are due to molecular transportation or reaction (production/depletion). A main mode of transportation is the random motion of molecules arising from thermal fluctuations; this is seen as diffusion in the continuum description. Diffusion causes the spread of localized signals and can be utilized for intra- or intercellular communication. In addition, reaction and enzymatic regulation are normally involved in the production, depletion, and diffusion of species. Molecular diffusion and enzyme reactions form a coupled system which is often associated with signal transduction, gene expression, and metabolism networks.

Another observation is that the diffusion in some biomolecular processes is driven by an electrostatic field induced by the environment. In these cases, the electrostatic interaction

can strongly affect the diffusion, and as a result, the rate of association between a ligand and receptor (e.g., see refs. 2 & 3). On the other hand, the electrostatic field is not only determined by the target macromolecule, but also by the density distributions of all the charged species, including diffusing ions and small charged molecules, which vary in time in nonsteady-state processes.

In the mean-field approximation, in which the particle-particle correlations of the diffusing molecules or ions are neglected, the Poisson-Nernst-Planck equation (PNPE) is a proper physical model to describe the coupling of electrostatics, density distribution, and diffusion processes. The PNPE is a combination of Nernst-Planck equations (NP) and Poisson equation (PE). The PE is used to describe the electrostatics in a medium induced by the charge distribution including both fixed and mobile charges. The NP is a current density equation widely used in studies of electrolyte transport and ion channels, as well as semiconductors. It is noted that another very similar and closely related equation is the Smoluchowski equation (SE), which is often used in studies of stochastic processes and kinetics of diffusion-reaction processes.⁴⁻⁷ The SE gives the conditional probability that the particle starting from the point $r(t_0)$ reaches the point r at the time t under influence of a potential. It describes the *diffusion of probability*, because the process of diffusion is the superposition of Brownian motions of the particles. In biological measurement, the current of ions (particles) contains a huge number of single ion passage events, which enable us to pass from one-ion description via probability density, i.e., from the SE, to the continuous description in terms of the electric current density, i.e., to the Smoluchowski-Nernst-Planck equation (continuity equation with the NP current, also simply called NP). Due to the similar mathematical formulas, the NP and the SE have same numerical structures. Differing from PNPE, the potential in the SE is normally considered as an external field that is not coupled with the (charged) diffusing particles. For instance, the electrostatic field is determined by the mean mobile ion density distribution, which obeys the Boltzmann distribution, then the SE in this case is referred to the Smoluchowski Poisson-Boltzmann equation (SPBE) in which the Poisson-Boltzmann equation (PBE) is solved only once, at the beginning, to supply the electrostatic field for the diffusion solution. Due to the uncoupling feature, the SPBE can be considered as a numerically simplified case of PNPE. Early

applications of SPBE solutions include theoretical studies of ion diffusion.^{8,9} Besides the aforementioned approximations, the application of the PBE assumes the ionic solution is in an equilibrium state. For nonsteady-state processes, or even steady-state processes with stationary values of diffusive fluxes (including ionic fluxes), the PE instead of the PBE must be used to determine the electrostatic field, because the non-equilibrium charge density distributions deviate from the Boltzmann distribution. This leads to the PNPE treatment. The usual application of the PNPE in biology is the steady-state version, which has been used extensively to investigate ion permeation and related transport processes with considerable success; for instance, in calculating the $I - V$ characteristics of ion channels. The numerical PNPE solvers are developed from 1D phenomenological model¹⁰⁻¹² to 3D PNPE solver for the protein ion channel permeation,¹³⁻¹⁶ and the comparison with 3D Brownian dynamics simulations are also performed.¹⁷⁻²⁰ Typically, a finite difference method (with exception of ref. 15 that used a spectral element method) has been used to approximate the solution in the membrane channel with either atomic-level resolution or using simplified descriptions.

The finite element (FE) version of the SPBE approach has been developed in previous work of our group and collaborators for the diffusion-controlled reaction of acetylcholine (ACh) in the neuromuscular junction (NMJ).²¹⁻²⁵ Solvers were developed for the time-dependent SE, with no interaction fields, for studies of the NMJ.^{21,22} Also, software was developed to solve the PBE using a multigrid method,²⁶ and this was used with the steady-state SE to study the consumption of ACh by acetylcholinesterase (AChE).^{24,25} The solution of the nonsteady-state SE for the above system is described in another work²⁷ and in this work. With the exception of ref. 21, each of these previous works, as well as the present work, makes use of the general finite element modeling library FETK,²⁸ developed over a number of years at UC San Diego.

The finite element method (FEM) has advantages in modeling irregular geometries with complex boundary conditions. In our finite element approach, the molecular surface (boundary) is identified and discretized; this discretization is used as the boundary of the volume mesh. Such meshes are said to be boundary or surface “conforming” because they are aligned with the “real” molecular surface, whereas in the finite difference method, the mesh is nonconforming because it is allowed to “cut through” the molecular surface. A 2D

comparison of the two types of meshes can be seen in Fig. 1. One consequence of adopting a nonconforming mesh is that sizable numerical errors in the solution are generated at the dielectric and permeability interfaces. Another advantage of adopting conforming mesh in our study is that it is convenient to use proper specification of boundary conditions on the surface for the modeling of reaction-diffusion processes.

In our scheme, the boundary-conforming mesh is also used in the boundary element method (BEM) to allow better predictions of the electrostatic field, especially at the molecular surface. It is standard practice to treat the charge distribution inside a large biomolecule as a collection of point charges. Using a finite-element method inside the molecule requires very fine meshing because of the singularities in the charge distribution, whereas the BEM handles such charge distributions very naturally using only surface elements. Although the interior of the large molecule still needs to be meshed in our hybrid FEM/BEM scheme, the volume mesh is not nearly as fine as would be required without the BEM.

(~ FIGURE 1)

The current work aims to integrate the former works and outlines a numerical framework to solve the complete PNPE, including both time-dependence and the coupling between the density of diffusing particles and electrostatics. In this framework, the time evolution of diffusion of each species is given, and the electrostatics is determined on-the-fly for each spontaneous configuration of charge distributions. The focus is on biological system with realistic geometry, especially at atomic resolution. In principle, the approach can be applied to systems with arbitrary numbers of diffusive species. Moreover, it also applies for both monovalent and multivalent ions (if the correlation effects are ignored), and it has the feature that no net charge neutrality is required for the system.

II. THE POISSON-NERNST-PLANCK EQUATION

A typical biophysical model is depicted in Fig. 2. The domain Ω_s denotes the solvent region where there is a mixed solution with one or more diffusive species, such as mobile ions

and small diffusing molecules. The domain Ω_m denotes the fixed macro-biomolecule(s), such as a protein, DNA, or membrane. In the following text, the whole computational domain is represented by $\Omega = \Omega_s + \Omega_m$. The diffusion region normally is limited to the domain Ω_s ; i.e., the moving particles are not allowed to penetrate into the region Ω_m . The continuum description of the diffusion of each species obeys the NP in terms of the current density. If one only considers the electrostatic interaction, the potential field can be generally described by the PE. Supposing q^i is the charge of each particle of the i th species, the coupled NP and Poisson equation system (PNPE), is

$$\begin{aligned} \frac{\partial p^i(r,t)}{\partial t} &= \nabla \cdot \{D^i(r)e^{-\beta q^i \phi(r,t)} \nabla (e^{\beta q^i \phi(r,t)} p^i(r,t))\} \\ &= \nabla \cdot \{D^i(r)(\nabla p^i(r,t) + \beta \nabla(q^i \phi(r,t)) p^i(r,t))\}, \quad r \in \Omega_s, \quad i = 1 \dots K, \end{aligned} \quad (1)$$

$$\nabla \cdot \varepsilon(r) \nabla \phi(r,t) = -\rho^f(r) - \sum_i q^i p^i(r,t), \quad r \in \Omega, \quad i = 1 \dots K, \quad (2)$$

where $p^i(r,t)$ is the density distribution function of the diffusing particles of the i th species with diffusion coefficient $D^i(r)$, ρ^f is the fixed source charge distribution (usually, the atomic charges of the biomolecule(s) in the system), K is the number of species considered, $\beta = 1/k_B T$ is the inverse Boltzmann energy, k_B is the Boltzmann constant, T is the temperature, ε is the dielectric coefficient, and ϕ is the electrostatic potential that imposes driving forces on the diffusing particles. When $p^i(r,t)$ is interpreted as the probability distribution function, Eq. (1) is the SE. Therefore, at some places in following sections in connection to our previous work, we also refer Eq. (1) to the SE.

It is worth noting that in Eqs. (1)-(2) all the charged species are treated as diffusing particles including the mobile ions that form the ionic solution. In some cases, if one is interested in the diffusion of larger particles such as substrates, and supposing that the density relaxation of the mobile ions is faster than the diffusion of the larger molecules, the distributions of the mobile ions can be considered to be in thermal equilibrium. That is, the ion densities can be approximated by the Boltzmann distribution $p^i = p_0^i e^{-\beta q^i \phi}$, where p_0^i is the bulk concentration of the i th ionic species. The advantage of this treatment is that the number of diffusion equations is then reduced by the number of these fast diffusing species. Eq. (2) is accordingly modified in this case. For example, for neutral 1:1 ionic

solution (monovalent ions), the electrostatic portion, Eq. (2), can be replaced with

$$\nabla \cdot \epsilon(r) \nabla \phi(r) - \lambda(r) \frac{\epsilon(r) \kappa^2(r)}{\beta} \sinh(\beta \phi(r)) + \rho^f(r) + \sum_i q^i p^i(r, t) = 0, \quad (3)$$

where κ is the inverse Debye length, $\lambda(r)$ is a function that is equal to 1 in regions where the counterions can penetrate, and 0 elsewhere, and the summation is only performed on the other species. The concentrations of the two counterions are implicitly included in the equation and do not appear in the diffusion equations. However, this treatment has the additional cost of solving a nonlinear PBE instead of a linear one in each coupling step. If no other diffusing species except mobile monovalent ions are in the solution, Eq. (3) is then the nonlinear Poisson-Boltzmann equation (NPBE):

$$\nabla \cdot \epsilon(r) \nabla \phi(r) - \lambda(r) \frac{\epsilon(r) \kappa^2(r)}{\beta} \sinh(\beta \phi(r)) + \rho^f(r) = 0. \quad (4)$$

A further simplified form, valid for small values of electric potential, is the linearized PBE (LPBE):

$$\nabla \cdot \epsilon(r) \nabla \phi(r) - \epsilon(r) \kappa^2(r) \phi(r) + \rho^f(r) = 0. \quad (5)$$

This can be very convenient in situations where the charges are not too strong. Because it is a linear partial differential equation, it can be solved using boundary element methods and treated just like the Poisson equation in the hybrid solution of Eqs. (1) and (2) described in the following sections.

(~ FIGURE 2)

III. NUMERICAL TREATMENTS

A. For the diffusion process

This work uses the Finite Element Toolkit (FETK), developed by two of the authors and collaborators²⁸ (<http://www.fetk.org/>), for the solution of the diffusion part, Eq. (1), around the macromolecule. For the case of no time-dependence (steady-state or equilibrium), the diffusion and electrostatic portions (Eq. (2) and Eq. (1)) are solved separately. Given an initial guess of the electric field ϕ , the diffusion portion of each species is solved using FETK. The resulting concentrations p_i are plugged into the electrostatic part, Eq. (2), which is solved, using the hybrid BE/FE method, described below, to obtain the electric field ϕ . The electric field is then plugged back into the diffusion equations Eq. (1) for the new concentration solutions. For the steady-state case, this process is repeated until the concentrations and electric field converge. For the time-dependent case, the diffusion portions, Eq. (1), are stepped forward in time, with the electric field solved at each time step for the input of next step solution of the diffusion equation using the hybrid method.

B. Electrostatic calculation

We have recently developed an efficient and accurate BEM solver for the linearized PBE by introducing a “node patch” BEM²⁹ and implementing the new version of the fast multipole method;^{30,31} this solver can be used for the PE as a special case. In principle, one could use the solver to solve the Poisson part, Eq. (2), using the charge distributions in both the solvent and macromolecule. However, including the solvent charge density would require volume integrals of the charge distribution over the entire domain. According to Boschitsch and Fenley,³² once volume integrals appear in the BEM the computation times incurred by a conventional, or even some multipole-accelerated integral equation methods, increase significantly and tend to be higher than even a finite-difference scheme of comparable accuracy. A hybrid finite difference/BEM approach and a decomposition strategy were adopted and tested to solve the nonlinear PBE in their work.³² So, rather than use boundary elements alone to solve the Poisson Equation, we use the hybrid BE/FEM

method described below to avoid the volume integrals.

In the hybrid FE/BE method, the strategy for solving Eqs. (2) and (1) is to decompose the solution of the Poisson equation into a singular component and a regular component, i.e., $\phi(r) = \phi^s(r) + \phi^r(r)$, The singular component is solved from the Poisson equation with singular charge distributions

$$\nabla \cdot \varepsilon(r) \nabla \phi^s(r) = -\rho^f(r), \quad r \in \Omega_m, \quad (6)$$

and the regular component is obtained by solving

$$\nabla \cdot \varepsilon(r) \nabla \phi^r(r) = \begin{cases} 0, & r \in \Omega_m, \\ -\sum_i q^i p^i(r), & r \in \Omega_s, \quad i = 1 \dots K. \end{cases} \quad (7)$$

The BEM is used in solving for the singular component, Eq. (6), and the FEM is used in solving for the regular component, Eq. (7). The splitting of the solution into singular and regular components was recently examined in detail theoretically for the Poisson-Boltzmann equation in ref. 33.

For a given macromolecule, the interior charge distribution is fixed; therefore, Eq. (6) is solved only once, at the beginning, to obtain the singular component ϕ^s , using the boundary element method. Afterwards, during each iteration between the diffusion and electrostatic equations for the non-time-dependent case, or for each time step for the time-dependent case, Eq. (7) is solved for the regular component ϕ^r . Because the charge density used for solving Eq. (7) is continuous in Ω_s and zero in Ω_m , the interior of the molecule does not need to be resolved with as fine a mesh as would be required for a FE solution to the singular component ϕ^s . In principle, the diffusion and regular electrostatic portions of the PNPE could be solved simultaneously using FETK, but the domains are different, with the diffusion part defined only on Ω_s ; this situation cannot be handled directly by the current version of FETK, but can be done as a block Gauss-Seidel iteration with FETK used to solve each block in a fixed-point iteration. We use the same mesh in Ω_s for solutions of both the diffusion and electrostatic equations, and apply a data transfer/mapping procedure

for the communication of charge densities and potentials between the coupled equations.

It is worth noting that when solving the PE in the whole domain Ω , the dielectric coefficient ϵ has different values in Ω_m and in Ω_s . This fact leads to the numerical difference between FD and BEM or FEM. In FD, the dielectric coefficient and the final solution at the interface are calculated through interpolation from the values at the neighboring grids, and the interface conditions are not enforced to be satisfied. While the boundary conforming mesh used here explicitly (in BEM) or implicitly (in FEM) satisfies the interfacing conditions, thus leads to better solutions at the interface. Comparison of the accuracy of the BEM solution can also be found in previous works.^{29,34}

For the case where the Poisson-Boltzmann approximation, Eq. (4), is used for the fixed electrostatic field (as in SPBE), the procedure is still the same, since FETK can be used to solve nonlinear equations. One just needs to include the nonlinear term of Eq. (4) in Eq. (7). In this case, the numerical method becomes essentially the one analyzed in ref. 33, with the singular component computed numerically rather than represented analytically.

C. Finite element treatment

A tetrahedral mesh is used to discretize the whole domain Ω , and the molecular surface is defined by a surface mesh of triangles that form faces of tetrahedra in both Ω_s and Ω_m . The same mesh in Ω_s is used to compute the solutions to the diffusion part, Eq. (1), and the regular electrostatic part, Eq. (7).

The numerical solution of NPBE, PE, or the steady-state SE involve the use of a fairly sophisticated adaptive method within FETK which is based on the use of error indicators to drive a SOLVE-ESTIMATE-MARK-REFINE iteration.^{28,33,35,36} Three core components of this adaptive solution algorithm in FETK, namely assembly of the linear and nonlinear algebraic equations, application of the discrete operators to vectors within iterative solution algorithms, and iterative inversion of the discrete operators inside a Newton iteration, also form the core computational kernels for the solution of time-dependent problems such as the time-dependent SE with updating of the electrostatic potential. Below we will first briefly review the methods for the steady-state problem, and then derive the algorithm for

the time-dependent PNPE system.

We now describe the mathematical framework employed in FETK for static and dynamics problems. Consider a general class of elliptic equations of the form:

$$-\nabla \cdot (D\nabla u) + b(u) + f = 0, \quad \text{in } \Omega_s, \quad (8)$$

$$u = \bar{u}|_{\partial\Omega_s}, \quad \text{on } \partial\Omega_s, \quad (9)$$

where D is a symmetric positive definite tensor, b is a real-valued function, f is a source term, its solution u also solves the following Galerkin weak problem

$$\text{Find } u \in \bar{u} + H_0^1(\Omega_s), \text{ such that } \langle F(u), v \rangle = 0, \quad \forall v \in H_0^1(\Omega_s), \quad (10)$$

where \bar{u} is a trace function satisfying the Dirichlet boundary conditions, $H_0^1(\Omega_s)$ is a Sobolev space of weakly differentiable functions which vanish on the boundary of the domain, and the ‘weak’ form $\langle F(u), v \rangle$, which generally is nonlinear in u and linear in v , is given by

$$\langle F(u), v \rangle = \int_{\Omega_s} (D\nabla u \cdot \nabla v + b(u)v + fv) dx. \quad (11)$$

In order to solve this nonlinear problem with a Newton-type iteration we need the directional derivative with respect to u in the direction of w of $\langle F(u), v \rangle$, which turns out to be a bilinear form

$$\begin{aligned} \langle DF(u)w, v \rangle &= \frac{d}{dl} \langle F(u + lw), v \rangle|_{l=0} \\ &= \int_{\Omega_s} (D\nabla w \cdot \nabla v + b'(u)wv) dx, \end{aligned} \quad (12)$$

where w is a test function. Note that if b is linear so that $b(u) = bu$, and $b'(u) = b$. Note that the boundary integrals vanish in the derivations of the above nonlinear weak and bilinear forms due to the fact that the test function, v , vanishes on the boundary. Denoting the approximate solution u by its expansion in the test function space, i.e., $u(x) = \sum_j a_j v_j(x)$, the weak form Eq. (11) essentially produces two matrices: a stiffness matrix A associated

with the product $D\nabla_w \cdot \nabla v$ and the mass matrix M associated with the product $b'(u)_{wv}$. The solution $u(x)$ of the weak form Eq. (11) is therefore equivalent to the solution of a linear algebraic system

$$(A + M)\vec{a} = -\vec{f}, \quad (13)$$

where unknown vector $\vec{a} = \{a_j\}$ is the expansion coefficients of u , and vector \vec{f} is known from the integration of $\int_{\Omega_s} f v dx$ for all given test functions v . Given the system of equations implied by Eq. (11) and the linearization Eq. (12), the FETK software solves them using *a posteriori* error estimation along with adaptive tetrahedron subdivision and unstructured algebraic multilevel methods for Eqs. (13) along with inexact Newton methods for Eq. (11). These methods within FETK have been shown to have linear space and time complexity for systems of the form Eqs. (13) and (11).

We now consider the time-dependent NP (or SE). For the NP of the i th species, defining $u = e^{\beta q^i \phi} p^i$ and $D' = D^i(r) e^{-\beta q^i \phi}$ gives rise to the symmetrized form of Eq. (1)

$$\frac{\partial}{\partial t}(u e^{-\beta q^i \phi}) = \nabla \cdot (D' \nabla u), \quad (14)$$

whose weak form is given by

$$\langle F(u), v \rangle = \int_{\Omega_s} D' \nabla u \cdot \nabla v - \beta q^i e^{-\beta q^i \phi} \frac{\partial \phi}{\partial t} u v + e^{-\beta q^i \phi} \frac{\partial u}{\partial t} v dx. \quad (15)$$

We use a time-dependent expansion, so called the method of lines

$$u(t, x) = \sum_j a_j(t) v_j(x)$$

and derive a governing equation to evolve the expansion vector $\vec{a}(t)$ from its given initial value. Indeed, by inserting the expansion $u(t, x) = \sum_j a_j(t) v_j(x)$ into Eq. (15) and using the matrix notation we could derive an equation similar to Eq. (13), as

$$A\vec{a} + cM\vec{a} + dM \frac{\partial \vec{a}}{\partial t} = 0, \quad (16)$$

where the three terms are the matrix representations of their corresponding terms in Eq. (15), $c = -\beta q^i e^{-\beta q^i \phi} \frac{\partial \phi}{\partial t}$ and $d = e^{-\beta q^i \phi}$. Here we assume that the derivative of electrostatic potential with respect to time $\frac{\partial \phi}{\partial t}$ at current time step is known when solving the NP. Eq. (16) provides the formulation to evolve the expansion coefficients \vec{a} from time step t_n to t_{n+1} :

$$\begin{aligned}\vec{a}_{n+1} &= \vec{a}_n + \int_{t^n}^{t^{n+1}} \frac{\partial \vec{a}}{\partial t} dt \\ &= \vec{a}_n - \int_{t^n}^{t^{n+1}} \frac{M^{-1}}{d} (A\vec{a} + cM\vec{a}) dt,\end{aligned}\quad (17)$$

where M^{-1} denotes the inverse of M . Different approximation methods can be used to numerically calculate the integral in Eq. (17), such as forward Euler method, backward Euler, or the Trapezoid rule. In this study, we use the backward Euler method because it is unconditionally stable and thus allows large time steps for the integration in Eq. (17). It does require inverting large sparse unstructured matrices, but we employ the low space and time complexity linear solvers in FETK to make these types of implicit methods competitive, or in the case of parabolic evolutions equations, substantially superior to explicit methods. With this backward Euler method and using a constant time increment $\Delta t = t_{n+1} - t_n$, we have

$$\begin{aligned}\vec{a}_{n+1} &= \vec{a}_n + \int_{t^n}^{t^{n+1}} \frac{\partial \vec{a}}{\partial t} dt \\ &= \vec{a}_n - \frac{M^{-1}}{d} (A\vec{a}_{n+1} + cM\vec{a}_{n+1}) \Delta t.\end{aligned}\quad (18)$$

Moreover, we define $\Delta \vec{a}_n = \vec{a}_{n+1} - \vec{a}_n$ so that we can compute \vec{a}_{n+1} by solving this $\Delta \vec{a}_n$ and adding it to \vec{a}_n . After some algebraic manipulations on Eq. (18) we get the following equation for $\Delta \vec{a}$:

$$\left(\frac{M}{\Delta t} + \frac{1}{d} (A + cM) \right) \Delta \vec{a}_n = -\frac{1}{d} (A + cM) \vec{a}_n.\quad (19)$$

This suggests that once we compute the first \vec{a}_0 from the initial condition on the concentration, we can iteratively solve Eq. (19) to calculate all the expansions \vec{a}_n , and hence the

concentration at any time t_{n+1} . The assembling of matrices A, M , and the solution of linear algebraic system Eq. (19) is accomplished by using the flexible numerical framework of FETK. The equations for computing $\Delta \vec{d}_n$ using the forward Euler method or the trapezoid rule can be derived similarly. In the case of implicit methods, the low complexity solver framework in FETK is used to solve Eq. (19).

For the steady-state NP, the time derivative parts vanish in the weak forms. The weak forms for the PE have the same form as the above NP's, and one only needs to substitute the time-dependent term with the charge distribution term.

D. Iteration procedure between the coupled NP and PE

For the steady-state case, in order for the iteration between the diffusion and electrostatic equations to converge, it was found necessary to employ underrelaxation, especially when macromolecule exists. In other words, variables were updated with a linear combination of old values and calculated new values, rather than just new values. The necessity of underrelaxation procedure was also experienced in the work of Corry et al.¹⁷ Even though, many iterations may be required in the non-time-dependent solutions. In the cases studied in this work, several tens or a few hundreds of iterations were required for convergence. The over-relaxation scheme has been used in the finite difference solver,¹³ but seems not applicable in this frame.

E. Boundary conditions

Proper boundary and/or initial conditions should be chosen according to different situations in applying the above equations. For the PE, because we normally choose a big enough domain Ω whose exterior boundary is far away from the molecule, the easily calculated Debye-Hückel screening potential on the boundary (induced by the total source charges) is taken as the (Dirichlet) boundary condition.

For the NP (or SE), if there is no absorption or source generation on the boundary for the diffusive particle, then either a reflecting boundary condition is used on the outside

boundary to simulate a closed box,

$$n(r) \cdot j = 0, \text{ for } r \in \Gamma_s,$$

or a Dirichlet boundary condition to simulate the bulk condition,

$$p(r) = p_{\text{bulk}}, \text{ for } r \in \Gamma_s.$$

The condition $j_n = 0$ is actually a Neumann condition for the pure diffusion equation, or, more generally, a type of Robin condition. On the molecular surface, it is also reasonable to use the reflecting boundary condition.

A special application is the solution of the diffusion-reaction system, which can be modeled by designating a “reactive” boundary patch Γ_a (see Fig. 2), and setting the boundary conditions as 24 & 37,

$$n(r) \cdot j = -k(r)p(r,t), \text{ for } r \in \Gamma_a,$$

$$n(r) \cdot j = 0, \text{ for } r \in \Gamma_m - \Gamma_a.$$

Such applications have been successfully performed on ACh consumption by the enzyme AChE, which is a diffusion-controlled reaction process.²⁴ In ref. 24, a simpler sink boundary condition is taken for the reaction site $p(r,t) = 0$, for $r \in \Gamma_a$.

The diffusion-influenced biomolecular reaction rate constant is calculated from the flux by integration over the active site boundary, as

$$k = \frac{-\int_{\Gamma_a} n \cdot j ds}{p_{\text{bulk}}}$$

IV. MESH GENERATION AND SYSTEM SET UP

Mesh generation is a long standing problem, hindering the wide application of the finite element and boundary element methods to biomolecular systems due to the very irregular shape of biomolecules. To enable our finite element modeling work using FETK, we

have built a high-quality biomolecular mesh generation toolchain using a number of existing mesh generation tools. The toolchain has essentially three main components. First, a triangulation of the solvent-excluded surface is generated using the program MSMS.³⁸ The molecular surface is the envelope of the atoms on the surface, represented as spheres with the atom's van der Waals radius. The surface atoms are determined by rolling a probe sphere with radius 1.4 Å over the surface; the atoms that are contacted by the probe sphere are considered part of the surface. The unaltered MSMS surface mesh could be used in the BEM calculation, but cannot serve as a boundary for the FE calculation because the triangulation contains many triangles with very small or large vertex angles, leading to large interpolation errors. This impacts both finite element and boundary element approximation quality. Therefore, in the second step, the program ADVENTURE_TetMesh³⁹ is used to smooth the surface triangular mesh. Finally, in the third step the tetrahedral volume mesh is generated using the program TetGen,⁴⁰ which starts with a closed triangulated boundary. In addition, if the domain is regular, as in a model system, the mesh can be generated using NETGEN.⁴¹ All of these tools are available freely online in source form, with the exception of MSMS which is only available as a binary executable.

Fig. 3 shows an example of the unstructured tetrahedral volume mesh and triangulated surface mesh of a fragment of A-form DNA used in our later FEM and BEM calculations. The molecular surface mesh is the smoothed version generated from the original surface mesh created by MSMS.

(~ FIGURE 3)

For the cases studied in this paper, AMBER force-field values were used for the partial atomic charges and van der Waals radii.⁴² The dielectric coefficient ϵ is set to 2 in Ω_m (molecular interior) and 78 in Ω_s (solution).

V. RESULTS

We mainly perform two types of calculations. First, the coupled system (PNPE) using Eqs. (1) and (2) in steady-state are solved for a spherical cavity model for illustrations, and for a DNA system to investigate the surrounding ionic density distribution. Second, using Eqs. (1) and (4), both the steady-state and time-dependent SE are solved using a pre-calculated PB potential (rather than then the coupled PE potential) in order to study the diffusion-reaction process.

A. Numerical accuracy test

A unit spherical cavity with a positive charge $+e$ located at the center was chosen to test the numerical accuracy of the FEM solution. A sphere with radius of 40 \AA was set as the outer boundary of the whole calculation domain. The whole volume mesh was generated with 22728 vertices and 111723 simplices (tetrahedra), of which 22704 vertices and 111311 simplices are located in the outside domain of the cavity. The FEM was used to solve Eq. (7) for the regular component of the electrostatic potential. Fig. 4 shows the relative errors of the calculated potentials (regular component) relative to the analytical one. The relative errors in the whole domain were kept at very small values. The increase in relative errors in the middle range of the radial distance was due to the mesh being coarser than in the other parts.

(\sim FIGURE 4)

B. Counterion compensation

Biological macromolecules are polyions whose function depends strongly on the surrounding ion atmosphere in solution. The accumulation of ions around oppositely-charged regions of the macromolecule is often called *charge compensation*, because the ions can

offset the charge on the macromolecule, sometimes even causing the charge around the molecule to reverse. Manning gave a suggested distance from the molecule to count for the counterion distribution and charge compensation.⁴³ In fact, from Gauss's law, the molecular charge must be compensated by ions to some distance far enough away from the molecule, because the electric field approaches zero, otherwise, the mobile counterions will move closer to compensate again. Therefore, the charge compensation could be used as a criterion for the accuracy of the continuum model for ion density prediction. We'll first revisit the theoretical predictions based on the solutions of the linearized Poisson-Boltzmann equation, Eq. (5). It is important to understand the approximation and its effect on computed charge compensation. The case of a charged sphere is a convenient system to study, because of the availability of analytical solutions.

For a unit sphere cavity of radius a with a point charge $-e$ located at the center, the LPBE potential is

$$\phi = \frac{-e \exp[-\kappa(r-a)]}{4\pi\epsilon_s(1+\kappa a)r}, \quad (20)$$

where $\kappa = \sqrt{2n_0e^2/(\epsilon_0k_B T)}$, ϵ_s is the solvent dielectric coefficient, and n_0 is the bulk ionic concentration. Then, the net charge $q(r)$ inside a volume of radius r , defined as the compensation charge, is the accumulation of the counterions and coions:

$$q(r) = \rho^+ + \rho^- = \int_a^r n_0[\exp(-\beta e\phi) - \exp(\beta e\phi)]dr^3. \quad (21)$$

The quantity $q(r)$ is numerically integrated using Matlab. It is worth noting here that Moy et al.⁴⁴ used again the linear approximation of the above Boltzmann distribution in Eq. (21) (this is the approximation used to get the LPBE from the NPBE) to derive an analytical solution:

$$q(r) = e\left[1 - \frac{1+\kappa r}{1+\kappa a} \exp(-\kappa(r-a))\right]. \quad (22)$$

We point out that these two formulas lead to essentially different pictures of charge compensation. Formula (22) predicts that the compensation charge within any radius monotonically increases but is bounded by $+1e$, corresponding to 100% compensation. This feature can be seen in Fig. 5a. However, formula (21) gives different compensation profiles for

different ionic strengths as shown by the blue curves in Fig. 5a. In particular, the curve at high ionic strengths may go beyond unity, indicating overscreening (charge reversal) of the cavity charge. At low ionic concentrations, the two formulas give similar predictions and do not show charge reversal within the distances shown in the figure. Fig. 5b gives a picture of the charge compensation within a fixed radius of 40 \AA with respect to the ionic strengths (through κ). The compensation has a peak at certain values of κ , but falls back to 100% again with an increase of κ . The figure shows the properties of counterion compensation from theoretical predictions, even though the large κ has no biological correspondence. Therefore, even using the linear PBE, the overscreening of counterions can be predicted by using Eq. (21).

In fact, if one extends the region of integration to be large enough in Fig. 5b, i.e., $> 40 \text{ \AA}$, it is found that the numerical integral results seem to always give over-screening even at very low ionic concentrations. This means that the direct solution of LPBE inherently overestimates the counterion densities. In the following section, we'll show that for the same spherical model the NPBE tends to give a smaller potential relative to that of LPBE, thereby leads to the prediction of a smaller counterion density. This indicates the improvement of the NPBE on charge compensation prediction, but it is still not proved that the NPBE solution leads to a monotonically increasing charge compensation and bounded by 100%.

(\sim FIGURE 5)

C. Solutions of the coupled system PNPE

C.1 Potential and ion density in equilibrium state

When there is no flux existing, the PNPE trivially reduces to the NPBE, Eqs. (4), with the charge density given by the Boltzmann factor. This property can be used to check the correctness of the PNPE program. We used a spherical cavity of radius 1 \AA to test

computations of the potential and charge compensation. One unit charge $+e$ was placed at the center, the interior of the sphere was set to a dielectric coefficient of 2, and the material outside the sphere (the solvent) was set to a dielectric coefficient of 78. A sphere with radius of 200 Å is set as the outer boundary of the computation domain. The volume mesh had 3745 vertices and 22614 simplices, in which 3721 vertices and 22206 simplices lie in the domain outside the cavity. The solvent contained a neutral 1:1 salt; 50 mM was set as the outer boundary condition for both positive and negative ions; and a reflecting boundary condition was imposed on the inner sphere. Comparisons among the potentials obtained with different numerical algorithms based on the LPBE, NPBE and PNPE are listed in Fig. 6.

It was found that the LPBE result nearly coincides with the exact, analytical solution. The results from the PNPE are very close to those from the direct solution of the NPBE, which is consistent with the model (the PNPE reduces to the NPBE at equilibrium). Thus, solving the PNPE at equilibrium provides another way to solve the NPBE. Deviation of the potential computed using the LPBE from that using the NPBE is found even at this low ionic concentration. Both the potentials from the NPBE and the PNPE are lower than the LPBE results, which is also reasonable from physical and mathematical analyses. The LPBE is more likely to overestimate the counterion screening effect as discussed in the above section. The resulting weaker potential leads to smaller computed compensation charges. The charge compensation, by integrating the total ion charge densities over the solvent domain, was computed to be 1.3, 1.1, and 0.98 e , using the numerical solutions of the LPBE, NPBE and PNPE, respectively. The differences in potentials and compensation charges between the results from the LPBE and the NPBE are expected to be larger with increased molecular charge or ionic concentration.

(~ FIGURE 6)

C..2 Effect of charge flux of a third diffusing species

Now we consider the same system, but with another diffusing species in addition to the 1:1 salt, with the third species being absorbed by the inner sphere (sink) at steady-state. The third species was given a plus or minus unit charge, and the spherical cavity boundary was set as a sink boundary ($p = 0$) to generate a charge flux. The outer boundary condition at $r = 200 \text{ \AA}$ for the third species was set to a 50 mM constant concentration. We explored the effect of the steady-state charge flux on the potential and concentration profile of the two ions, and vice versa, the effect of the coupling among the three charged species to the flux expressed by rate constant. Both positively and negatively charged reacting species were considered. The results are shown in Fig. 7.

(~ FIGURE 7)

It was found in Fig. 7a that the potential and the density distributions of both counterions and coions of salt were significantly affected even at a modest 50 mM ionic strength. The positively (negatively) charged flux raised (lowered) the potential throughout the whole domain. This effect was seen because the reacting species added its own charge to the system. In this case, the potential shift was on the scale around 0.2 kcal/mol·e. It was even seen that the negatively charged flux could lead to reversal of the the total potential sign at certain distances; this would not happen in the 1:1 salt using the NPBE model for the ions. Fig. 7b-c show the significant changes in the counterion and coion density distributions caused by the charged flux. The magnitude of changes was about one third of the original, unperturbed profile.

The calculations with different models also showed obvious effects of the coupling of the three charged species to the reaction rate constant. For example, in the SPBE model, the negative flux had a rate constant of $3.17 \times 10^{11} \text{ M}^{-1} \text{ min}^{-1}$, while in the PNPE model it decreased to $2.39 \times 10^{11} \text{ M}^{-1} \text{ min}^{-1}$, and $2.82 \times 10^{11} \text{ M}^{-1} \text{ min}^{-1}$ if the the bulk concentration of the third species was 10 mM. This indicates that the higher concentration of the reactive species, the stronger effect of the coupling will be imposed on the rate constant.

To further check how the interaction between the reactive particles affects the rate constant, we set the ionic strength to zero, and it was found that the calculated rate constant was $3.84 \times 10^{11} \text{M}^{-1} \text{min}^{-1}$ in SPBE, $2.50 \times 10^{11} \text{M}^{-1} \text{min}^{-1}$ in PNPE for a bulk concentration of 50 mM of the diffusing particle, and $9.87 \times 10^{10} \text{M}^{-1} \text{min}^{-1}$ in PNPE for a bulk concentration of 300 mM of the diffusing particle. This implies that the strongly electric repulsion between the reactive particles leads to great reduction in rate constant. A simple explanation underlies here for this phenomena. According to Gauss's law for the simple symmetric sphere case, the diffusing particles surrounding the sphere associated with the flux induce a repulsive drifting field for the diffusion, which lowers the rate coefficient compared with the case with the repulsion interaction ignored. Therefore, the inter-particle repulsion and the sink-particle attraction are competitive factors to the rate constant, and both are regulated (reduced) by ionic strength. For this reason, the reaction rate coefficient can be expected to be increased by the ionic screening due to the weakened inter-particle repulsion in certain ranges of ionic and diffusing particle concentrations. For instance, with a bulk concentration of 300 mM for the diffusing particle, the rate constant in PNPE calculation at 50 mM ionic strength is $1.35 \times 10^{11} \text{M}^{-1} \text{min}^{-1}$, which is higher than that in case of zero ionic strength as shown above. This observation actually discloses a violation of the widely accepted rate theory based on the famous Debye-Hückel law (e.g., see ref. 3).

These results demonstrate the significance of the effects of mutual interactions among salt ions and other charged diffusing particles. Furthermore, they highlight the importance of solving the coupled PNPE, rather than the SPBE, especially in cases of large flux. However, the SPBE is still an acceptable approximation of the PNPE when the concentration of the reacting species is small and then the coupling is not strong (at zero ionic strength, $\sim 10\%$ difference in the rate constants obtained with the two methods at 10 mM, and $\sim 1.4\%$ at 1 mM). This approximation is desirable when possible because of the large savings in computational cost.

C..3 Ion density around the DNA

We calculated the ion distributions around a fragment of A-form DNA with 12 base pairs and a net charge of $-22e$. The system has a strong negative potential field, which attracts cations. The system was bounded on the outside by a spherical boundary with a radius of 200 \AA . The mesh over the whole domain had a total of 99093 vertices and 620117 simplices, with 24503 vertices and 49002 triangles on the molecular surface, and 74163 vertices and 388419 tetrahedra in the solvent domain. For comparison, we calculated concentrations of both monovalent (i.e., Na^+) and divalent (i.e., Ca^{2+}) cations. The bulk densities in solution for, i.e., NaCl and CaCl_2 , were set to 50 mM and 25 mM, respectively. Fig. 8 shows the surface potential and the counterion concentrations around DNA. Fig. 8a shows a common feature of A-form DNA - a strongly negative electrostatic potential in the major groove. This led to the dense concentration of cations in the major groove (see Fig. 8b-c). When the solution was changed to CaCl_2 , the bivalent Ca^{2+} ions were much more strongly attracted to the major groove (Fig. 8b) than the monovalent cation, and the highly concentrated regions were larger. This observation agrees with the known fact that the bivalent cation binds much more strongly (far greater than a factor of two) than the monovalent cation to the site with negative potential. In addition, the calculations predicted very accurately charge compensations in the whole exterior domain of DNA: $21.3e$ (1013.7 Na^+ , 992.4 Cl^-) for 1:1 salt and $21.1e$ (508.0 Ca^{2+} , 994.9 Cl^-) for 2:1 salt.

(~ FIGURE 8)

D. Solutions of the uncoupled system SPBE

D..1 Steady state diffusion-reaction system—ACh consumption

Debye-Hückel theory predicts the screening effect of mobile ions in solution on the electrostatic potential of immersed biomolecules. This theory implemented within transition state theory gives a similar screening effect (exponentially decreasing with ion concen-

tration) on the rate of protein-protein or protein-ligand association, which is called the Debye-Hückel limiting law. Because of consistency in principle, the SPBE model can be expected to reproduce the behavior following the Debye-Hückel limiting law. The basic ionic-strength dependence of the binding rate can also be found by combining Zhou's average Boltzmann factor theory and the screened electrostatic potential approximation.^{45,46} The Debye-Hückel limiting law was used to fit the experimental data of ligand binding to acetylcholinesterase.³ Former papers^{24,25} studied the steady-state reaction rate of the AChE monomer with acetylcholine in SPBE model, using the software package APBS²⁶ to compute the potential with non-adaptive and adaptive meshes. To compare, we repeated the calculation using the Poisson-Boltzmann potential computed from the boundary-element method. All of the simulations in the AChE studies, both steady-state and the time-dependent cases, were done by solving the linearized PBE for the mobile ions only once at the start, plugging the electric field into Eq. (1), and then solving the SE for the ACh concentration.

ACh is a positively charged ligand, and a diffusivity of $D(r) = 78000\text{\AA}^2/\mu\text{s}$ is assumed for ACh and a neutral ligand (TFK⁰) for later comparison. Rather than using the procedure described above for generating meshes, we chose to use the same meshes for the AChE monomer and tetramer as were used in the previous works^{24,47} in order to facilitate comparison of results. The meshes were generated only for the solvent domain Ω_s , and not for the interior of AChE, which allows solution of the SPBE problem but not the PNPE in current frame as described in the previous sections. The tetrahedral mesh sizes for the AChE monomer were 312, 276, and 366 nm for the lengths of the three principal axes respectively, and that for the AChE tetramer (1c2b) were 763, 671, and 679 nm. These sizes were about 40 times the radius of the monomer. More details about the meshes and the boundary conditions can be found in refs. 24 and 47.

It is worth noting that AChE densities at vertebrate neuromuscular junction range from $2000\sim 3000/\mu\text{m}^2$, both in the primary cleft and in the secondary cleft folds,^{48,49} depending on the species. This is approximately equivalent to 20 nm of separation for a square array distribution. AChE appears in the NMJ mainly in a cluster of 3 tetramers. Thus, the mesh sizes were several times larger than the separation between AChE molecules; we did not

attempt to address the issue of competition among neighboring AChE molecules *in vivo*. If the steady-state reaction rate is computed, as in the former works,^{24,25,47} the radius of the outer boundary does not significantly affect the results, because the boundary condition on the outer boundary is set to the bulk density. This is a good approximation when the outer mesh boundary is sufficiently far from the molecule. As in the previous studies, we used a Dirichlet condition on the outer boundary with values of the bulk concentrations, reflecting boundary conditions on most of the molecular surface, and an absorbing boundary condition at the active site.

Fig. 9 shows that both approaches correctly captured the screening effect of ionic solution on the binding rate of the charged substrate, and agreed well with the fit of the Debye-Hückel limiting law to the experimental data. Because the computed reaction rate is directly affected by the electric potential at the active site, the more accurate value of the potential computed from the BEM gives improved rates over even the refined FE mesh from the previous studies.

(~ FIGURE 9)

D.2 Time dependent diffusion reaction process

The time-dependent case gives more kinetic information on the diffusion-reaction process than does the steady-state case. However, it strongly relies on the initial condition, locations and types of boundary conditions, and the mesh geometry. For instance, in the steady-state situation, the calculated reaction rate constant is not sensitive to the boundary value and the size of the outer boundary (if far enough away from the molecule), whereas in time-dependent case, all of these factors do affect the observations. Therefore, results such as the ACh depletion time, cannot yet be compared directly to experimental data, but can supply important qualitative information on properties and factors affecting the process, if the conditions closely approximate conditions *in vivo* or *in vitro*.

In each calculation, there was one AChE monomer or tetramer located at the center of the mesh. A reflecting boundary condition on the outside boundary of the mesh was used to avoid the spreading of ACh to a much larger volume. Two types of initial conditions were used. One was a uniform distribution of ACh in the whole diffusion domain around AChE; this is based on the assumption that ACh quickly fills the synaptic cleft after release from the vesicle, compared to the time scale of whole synaptic activity and depletion. The other is a pulse of ACh corresponding to about 10,000 molecules of ACh at about 0.3 M concentration, uniformly distributed in a sphere 24 nm in radius, and centered 48 nm from the enzyme center on the positive y-axis. The latter pulse condition roughly corresponds to what happens in the neuromuscular junction (NMJ)^{21,22,50-52} upon release of ACh from a synaptic vesicle (represented by the sphere) in the frog NMJ.⁵³ The reactive boundary on molecular surface is also equipped with Dirichlet condition, and with zero value to reflect the fast catalytic process which clears the ACh from the NMJ. We note that the AChE density in this circumstance is lower than in real NMJ as mentioned in the mesh generation section, and interactions among the ACh molecules were neglected. However, the model still gives useful information about the time scales and trends of ACh depletion.

(~ FIGURE 10)

Fig. 10 is a set of visualizations of the diffusion-reaction processes for the cases with monomer or tetramer of AChE, positively charged or neutral diffusing substrate, and different initial conditions. The salient feature is the ability of the electrostatic field of the enzyme AChE to steer ACh diffusion by absorbing it to the peripheral sites of the reactive gorge of AChE even at very early times (see Fig. 10d at 0.1 μ s and Fig. 10h at 0.5 μ s) to accelerate the reaction. However, the initial ACh pulse quickly spreads in the whole space even when perturbed by the electrostatic attraction (see Fig. 10e and h). Under normal physiological conditions, it appears that the initial pulse of ACh reaches a fairly even distribution in a short time, and then the electrostatic forces persistently steer the substrate molecules to the active site. In other words, a quasi-steady-state condition is established with the rapid initial spread of substrate, followed by the slower channeling to the active

site. This effect is seen in the graphs of Fig. 11, showing a slow decay in numbers of remaining ACh after a rapid transient. This holds even for the case of small ionic concentration, where the steering effect is greatest.

(~ FIGURE 11)

Fig. 11a shows the consumption kinetics of an initial ACh and TFK⁰ pulse by the AChE monomer under different ion strengths. It can be observed that higher ionic strengths cause higher build-ups of ACh due to electrostatic screening, but the electric field still accelerates the reaction rate several-fold, compared to the case of the neutral substrate. The time required to consume one half of the total ACh in solution of 0 mM ionic strength is just about one eighth ($350 \mu\text{s}/2620 \mu\text{s}$) of the time required at 300 mM ionic strength.

Fig. 11b plots the consumption rate of AChE in the early stage of the process. In the following longer depletion period, each line smoothly declines in a slower exponential decay. The time for the reaction rate to reach the maximum value reflects the effect of the substrate-enzyme interaction on the diffusion. Using a reference time scale estimated from the Einstein-Smoluchowski equation, $\langle r^2 \rangle = 6Dt$, the average time for a particle to freely diffuse across 45 nm, a distance between the vesicle center and the AChE reactive site, is $0.43 \mu\text{s}$. This is close to the neutral case (Fig. 11b, purple line). In the charged cases, the times to reach the maximum are a bit greater than in the neutral case, and the magnitudes increase significantly. A direct explanation is that the electrostatic attraction helps to gather more ACh molecules (increased magnitude), and from a longer range (delayed peak), into the AChE reactive site than does the free diffusion.

We also set the initial pulse position at different directions from the enzyme but at the same distance. We found that this affected the overall ACh depletion process very little (data not shown here).

(~ FIGURE 12)

Fig. 12 shows the results of the simulations with initial condition of an ACh bulk $\rho(r, 0) =$

1. Because Eq. (1) is linear with respect to density p , the initial bulk density will not affect the dynamic features, so all numbers of residual ACh molecules are normalized. In this case it is found that ACh consumption processes show the same tendency as seen in Fig. 11.

VI. CONCLUSIONS AND DISCUSSION

A numerical framework has been developed to enable the simulation of the electrodiffusion process in biomolecular systems. The framework consists of a biomolecular modeling toolchain and a boundary element solver combined with the FETK finite element modeling library for both statics and dynamics. The quality of the generated meshes is sufficient for the present finite element calculation, and the hybrid scheme is validated by the results. The program gives accurate calculations for the potential profile, density distribution, and compensation charges for different models (linearized PBE, nonlinear PBE, PNPE). The calculation results for the unit spherical model also indicate that even at 50 mM concentration of the diffusing particle the coupling among all the charged species in the diffusing system significantly affects the reaction rate, so application of the PNPE is recommended for reaction rate calculations if sufficient computational resources are available. The time-dependent model (currently still an uncoupled system) can capture the main features of the consumption of the substrate ACh, as well as TFK⁰. The detailed geometry of AChE, electrostatics, and ionic strength are included in this model, and the time scale represented by the computation can reach microseconds to milliseconds. This is on the same time scale as phenomena in the synapse, allowing the possibility of predicting and comparing with experimental measurements.

The current program incorporates the solvers of the linear and nonlinear PBEs, NP/SE, and their coupled/uncoupled forms (PNPE/SPBE), allowing for the treatments of a variety of continuum models. This methodology can be applied to the other fields as well, like colloid science, with dimensions scaled accordingly. Although representing an improved algorithm, the program is comparable with the previous work using FETK²⁴ but using other mesh generation tools, and the electric potential fields used as input can be generated from

the APBS package. In addition, in order to reduce the complexity of the program package, both the SE and the PE can be solved using the FETK package alone, but a procedure is required to generate a fine enough interior mesh for the macromolecule to guarantee numerical accuracy.

As with all models based on continuum descriptions of ions, such as the Poisson-Boltzmann equation, the biggest room for improvement is in the model itself. The current PNPE is based on the mean field approximation, in which finite ion size or ion-to-ion correlation is not considered. Such effects cause ion saturation in highly charged systems like DNA and single filing of ions in channels; these phenomena cannot be captured by the present continuum model. For example, ion concentrations are overestimated near charged surfaces in comparison with models in which the ions are explicitly included in, e.g., Brownian dynamics⁵⁴ or grand canonical Monte Carlo simulations.⁵⁵ Some recent models have been proposed and tested in ion channel permeation to effectively take into account the ion size,^{56,57} thus partially remove the limitation that mobile species are treated as point charges. Another effect neglected by these models is the specific interactions of some ions, such as Mg^{2+} , with water and their influence on the water's microstructure. For example, the Mg^{2+} ion is typically accompanied by several water molecules, even when bound to DNA or proteins. Moreover, current work completely ignores molecular flexibility and the presence of thermal noise, a macromolecule flexibility could play important role in the process of ion density relaxation. It may be useful to take into account the macromolecular flexibility into the PNPE theory to calculate fluxes and mobile ion density distribution. A recent work incorporates information about the channel dynamics in terms of potential of mean force into PNPE calculation.⁵⁸ Another possible way is to extract a set of snapshots (ensemble) from the trajectory of molecular dynamics simulation, then perform PNPE calculation for each conformation and analyze the results. This type of work is underway to study the catalysis efficiency for the dynamical AChE tetramers.

Several improvements could be made in the numerical solution itself. As mentioned above, the underrelaxation iterative procedure for the PNPE in our FE frame seems necessary, especially when macromolecule exists. However, such iteration procedure might be difficult to converge in cases of highly charged macromolecular systems, and need to be

improved. Where possible, one should use the Poisson-Boltzmann approximations to avoid the iterative solution. Work is underway to carry out a FEM computation on the regular component of the electrostatic solution, Eq. (7), in which the interior of the biomolecule does not need to be meshed; this will allow simultaneous solution of both diffusive and electrostatic components using FETK because the meshes will coincide. Finally, the current boundary condition settings for the PE solution may not be completely correct for the cases where three or more types of diffusing particle exist or if the whole system is far from neutrality.

For the solution of time-dependent PNPE, it is expected that the CPU cost would be increased by several times compared with that of the solution of pure diffusion equation or SPBE, depending on the total number ($K + 1$, K is the number of diffusing species) of equations to be solved at each time step. This is still acceptable for normal computational power.

Despite the above limitations, the Poisson-Nernst-Planck model and the software framework can give accurate values for charged particle density and reaction rates, provided that the particles are dilute and the strength of the electric field is not too high.

ACKNOWLEDGEMENTS

We'd like to thank Jason Suen for his previous work coding an interface to FETK, Nathan Baker for his comments and suggestions, Xiaolin Cheng for his help with BEM, and Deqiang Zhang for AChE meshes. The work was supported in part by the NIH, NSF, the Howard Hughes Medical Institute, National Biomedical Computing Resource, the NSF Center for Theoretical Biological Physics, SDSC, the W. M. Keck Foundation, and Accelrys, Inc. Michael Holst was supported in part by NSF Awards 0411723, 0511766, and 0225630, and DOE Awards DE-FG02-05ER25707 and DE-FG02-04ER25620.

References

1. R. Y. Tsien, *Nat. Cell Biol.*, SS16 (2003).
2. F. B. Sheinerman, R. Norel, and B. Honig, *Curr. Opin. Struct. Biol.* **10**, 153 (2000).

3. Z. Radic, D. M. Quinn, J. A. McCammon, and P. Taylor, *J. Biol. Chem.* **272**, 23265 (1997).
4. M. Smoluchowski, *Z. Phys. Chem.* **92**, 129 (1917).
5. S. Chandrasekhar, *Rev. Mod. Phys.* **15**, 1 (1943).
6. S. A. Rice, Diffusion-limited reactions, in *Comprehensive chemical kinetics*, edited by C. H. Bamford, C. F. H. Tipper, and R. G. Compton, volume 25, Elsevier, Amsterdam, 1985.
7. A. Szabo, *J. Phys. Chem.* **93**, 6929 (1989).
8. S. Lifson and J. L. Jackson, *J. Chem. Phys.* **36**, 2410 (1962).
9. D. Y. C. Chan and B. Halle, *Biophys. J.* **46**, 387 (1984).
10. H. Cohen and J. W. Cooley, *Biophys. J.* **5**, 145 (1965).
11. R. Eisenberg and D. P. Chen, *Biophys. J.* **64**, A22 (1993).
12. R. S. Eisenberg, *J. Membr. Biol.* **150**, 1 (1996).
13. M. G. Kurnikova, R. D. Coalson, P. Graf, and A. Nitzan, *Biophys. J.* **76**, 642 (1999).
14. A. E. Cardenas, R. D. Coalson, and M. G. Kurnikova, *Biophys. J.* **79**, 80 (2000).
15. U. Hollerbach, D. P. Chen, D. D. Busath, and B. Eisenberg, *Langmuir* **16**, 5509 (2000).
16. S. Furini, F. Zerbetto, and S. Cavalcanti, *Biophys. J.* **91**, 3162 (2006).
17. B. Corry, S. Kuyucak, and S. H. Chung, *Biophys. J.* **78**, 2364 (2000).
18. S. Berneche and B. Roux, A microscopic view of ion conduction through the k⁺ channel, in *Proc. Natl. Acad. Sci. U. S. A.*, pages 8644–8648, 2003, Published as *Proc. Natl. Acad. Sci. U. S. A.*, volume 100, number 15.
19. S. Y. Noskov, W. Im, and B. Roux, *Biophys. J.* **87**, 2299 (2004).
20. B. Roux, T. Allen, S. Berneche, and W. Im, *Q. Rev. Biophys.* **37**, 15 (2004).

21. J. L. Smart and J. A. McCammon, *Biophys. J.* **75**, 1679 (1998).
22. K. S. Tai, S. D. Bond, H. R. Macmillan, N. A. Baker, M. J. Holst, and J. A. McCammon, *Biophys. J.* **84**, 2234 (2003).
23. Y. Cheng, J. Suen, Z. Radic, S. Bond, M. Holst, and J.A. McCammon, *Biophys. Chem.* **127**, 129 (2007).
24. Y. H. Song, Y. J. Zhang, T. Y. Shen, C. L. Bajaj, J. A. McCammon, and N. A. Baker, *Biophys. J.* **86**, 2017 (2004).
25. Y. H. Song, Y. J. Zhang, C. L. Bajaj, and N. A. Baker, *Biophys. J.* **87**, 1558 (2004).
26. N. A. Baker, D. Sept, S. Joseph, M. J. Holst, and J. A. McCammon, *Proc. Natl. Acad. Sci. U. S. A.* **98**, 10037 (2001).
27. Y. Cheng, J. K. Suen, D. Zhang, S. D. Bond, Y. Zhang, Y. Song, N. A. Baker, C. L. Bajaj, M. J. Holst, and J. A. McCammon, *Biophys. J.* (in press).
28. M. Holst, *Advances in Computational Mathematics* **15**, 139 (2001).
29. B. Z. Lu and J. A. McCammon, *J. Chem. Theory. Comput.* **3**, 1134 (2007).
30. L. F. Greengard and J. F. Huang, *J. Comput. Phys.* **180**, 642 (2002).
31. B. Z. Lu, X. L. Cheng, J. F. Huang, and J. A. McCammon, *Proc. Natl. Acad. Sci. U. S. A.* **103**, 19314 (2006).
32. A. H. Boschitsch and M. O. Fenley, *J. Comput. Chem.* **25**, 935 (2004).
33. L. Chen, M. Holst, and J. Xu, The finite element approximation of the nonlinear Poisson-Boltzmann Equation, Submitted to *SIAM J. Numer. Anal.*
34. B. Z. Lu, D. Q. Zhang, and J. A. McCammon, *J. Chem. Phys.* **122**, 214102 (2005).
35. R. Bank and M. Holst, *SIAM Rev.* **45**, 291 (2003).

36. M. Holst, Applications of domain decomposition and partition of unity methods in physics and geometry (plenary paper), in *Proceedings of the fourteenth international conference on domain decomposition methods, Cocoyoc, Mexico*, edited by I. Herrera, D. Keyes, O. Widlund, and R. Yates, Domain Decomposition Methods in Science and Engineering, pages 63–78, Mexico City, Mexico, June 2003, National Autonomous University of Mexico (UNAM).
37. H. X. Zhou, *J. Phys. Chem.* **94**, 8794 (1990).
38. M. F. Sanner, A. J. Olson, and J. C. Spehner, *Biopolymers* **38**, 305 (1996).
39. G. Yagawa, S. Yoshimura, and K. Nakao, *Integrated Computer-Aided Engineering* **2**, 265 (1995), software: ADVENTURE_TetMesh.
40. H. Si and K. Gaertner, Meshing piecewise linear complexes by constrained Delaunay tetrahedralizations, in *Proceedings of the 14th International Meshing Roundtable*, pages 147–163, 2005, software: Tetgen.
41. J. Schöberl, *Comput. Visual Sci.* **1**, 41 (1997).
42. W. D. Cornell, P. Cieplak, C. I. Bayly, I. R. Gould, K. M. Merz, D. M. Ferguson, D. C. Spellmeyer, T. Fox, J. W. Caldwell, and P. A. Kollman, *J. Am. Chem. Soc.* **117**, 5179 (1995).
43. G. S. Manning, *Q. Rev. Biophys.* **11**, 179 (1978).
44. G. Moy, B. Corry, S. Kuyucak, and S. H. Chung, *Biophys. J.* **78**, 2349 (2000).
45. H. X. Zhou, *J. Chem. Phys.* **105**, 7235 (1996).
46. H. X. Zhou, *Biopolymers* **59**, 427 (2001).
47. D. Q. Zhang, J. Suen, Y. J. Zhang, Y. H. Song, Z. Radić, P. Taylor, M. J. Holst, C. Bajaj, N. A. Baker, and J. A. McCammon, *Biophys. J.* **88**, 1659 (2005).
48. M. M. Salpeter, A. W. Rogers, H. Kasprzak, and F. A. Mchenry, *J. Cell Biol.* **78**, 274 (1978).

49. L. Anglister, J. R. Stiles, B. Haesaert, J. Eichler, and M. M. Salpeter, Acetylcholinesterase at neuromuscular junctions: density, catalytic turnover, and molecular forms with modeling and physiological implications, in *Enzymes of the Cholinesterase Family*, edited by D. M. Quinn, A. S. Balasubramanian, B. P. Doctor, and P. Taylor, chapter IV, pages 277–285, Plenum Press, New York, 1995.
50. J. H. Schwartz, Synaptic vesicles, in *Principles of Neural Science*, edited by E. R. Kandel, J. H. Schwartz, and T. M. Jessell, pages 225–234, Appleton and Lange, Norwalk, Connecticut., 1991.
51. H. Zimmermann, *Synaptic Transmission: Cellular and Molecular Basis*, Thieme, Stuttgart, Germany, 1993.
52. T. C. Südhof and R. H. Scheller, Mechanism and regulation of neurotransmitter release., in *Synapses*, Johns Hopkins University Press, Baltimore, Maryland., 2000, W. M. Cowan, T. C. Südhof, and C. F. Stevens, editors.
53. W. Van der Kloot, J. Molgo, R. Cameron, and C. Colasante, *J. Physiol.-London* **541**, 385 (2002).
54. B. Corry, S. Kuyucak, and S. H. Chung, *Biophys. J.* **84**, 3594 (2003).
55. A. Vitalis, N. A. Baker, and J. A. McCammon, *Mol. Simul.* **30**, 45 (2004).
56. P. Graf, M. G. Kurnikova, R. D. Coalson, and A. Nitzan, *J. Phys. Chem. B* **108**, 2006 (2004).
57. Z. Schuss, B. Nadler, and R. S. Eisenberg, *Phys. Rev. E* **6403** (2001).
58. A. B. Mamonov, R. D. Coalson, A. Nitzan, and M. G. Kurnikova, *Biophys. J.* **84**, 3646 (2003).
59. OpenDX, <http://www.opendx.org>.

VII. FIGURE CAPTIONS

FIGURE 1 An example of conforming and nonconforming 2D meshes. The molecular interior is represented by shading, and the mesh covers the whole domain in each case.

FIGURE 2 Schematic of problem domain, denoting the boundaries and volumes. Γ_m denotes the fixed molecular boundary, and Γ_s is the boundary of the whole volume mesh. If reaction on the molecular surface is considered, according to Song et al.'s treatment²⁴ (similar figure can also be found therein), a small patch Γ_a ($\Gamma_a \subset \Gamma_m$) around the active site is set to a zero Dirichlet boundary condition (sink boundary) to model the chemical reaction.

FIGURE 3 An example of mesh generation for a fragment of A-form DNA. (a) Cross-section of the whole tetrahedral volume mesh. (b) A close-up view of the fine mesh around the molecule, whose body is colored by green. The edge between green and blue regions lies on the molecular surface. (c) The triangular boundary mesh conforming to the molecular surface.

FIGURE 4 The numerical error in the solution of the regular part of the PBE using FEM.

FIGURE 5 The charge compensation predicted based on the analytical solution of the LPBE for a unit sphere cavity with charge $-e$ at the center. (a) The compensation charge as a function of radial distance at different ionic strengths represented by κ . Blue lines correspond the results from Eq. (21), red marks from Eq. (22). (b) The net charge within $r = 40\text{\AA}$ as a function of κ using Eq. (22) (red) and Eq. (21) (blue).

FIGURE 6 Comparisons of the calculated electrostatic potentials in 50 mM 1:1 salt around a unit spherical cavity with $+e$ at the center from different approaches: the analytical LPBE solution (blue square), LPBE (black star), NPBE (red triangle), and PNPE (green circle).

FIGURE 7 Effects of the addition of a charge flux in the 50 mM 1:1 salt to (a) the po-

tential, (b) the counterion and (c) the coion density distributions. In three figures, the red square marks denote the 1:1 salt case without charge flux, the blue triangle marks denote the case with a negative charge flux ($-e$ particle) added in the salt, the black star the case with a positive charge flux added in the salt.

FIGURE 8 Electrostatic potential and cation density (mM) around a fragment of A-form DNA. (a) Surface electrostatic potential from the BEM LPBE solution in a 50 mM 1:1 salt. The color scale is from -11 (red) to 10 (blue) kcal/mol.e. (b) Cross-section of the density distribution in 50 mM 1:1 salt. (c) Density distribution in 25 mM 2:1 salt (e.g, CaCl_2). The color scale is doubled for ease of comparison with (b). (d) Density isosurface with a value of 3000 mM in the case (b) from a different orientation. These and all the following density figures are generated using the software OpenDX.⁵⁹

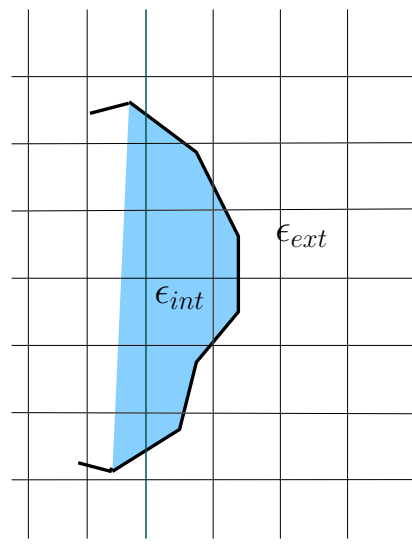
FIGURE 9 Comparison of calculations of the steady-state reaction rate of AChE monomer with BEM potential, APBS potential, and experimental fitting data. The dotted lines are the results from ref. 25 with APBS electrostatic potential using unrefined or refined meshes, respectively. The thin solid line is from experimental data³ fit to the Debye-Hückel limiting law.

FIGURE 10 Visualization of the evolution of substrate concentrations in the diffusion-reaction processes. $+e$ denotes the one unit positively charged ligand ACh, $0e$ denotes the neutral ligand TFK⁰. Figures (a)-(g) show the cases of diffusion from an initial pulse in the presence of AChE monomer at ionic strength 0.3 M. Figure (h) shows the tetramer (1c2b) case with diffusion with an initial condition of ACh pulse and in zero ionic strength. Figure (i) is the same as (h), but with a uniform distribution (0.3 M) of ACh as the initial condition. For the sake of visualization, different color scales are used in different subfigures. The largest color scales (red) are 0.00018 in figures (a)-(c), and 0.0001 in (d), 0.00005 in (e)-(h), and 1.0 in (i).

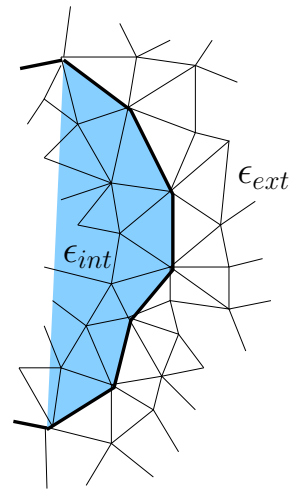
FIGURE 11 Substrate consumption processes by AChE monomer at different ionic strength.

+e denotes the positively charged ACh, 0e the neutral TFK⁰. The diffusion starts from a vesicle-sized area containing 10000 ACh molecules and ~ 20 nm away from AChE (see Fig. 10a). The bottom figure shows a close-up view of the transient behavior at the beginning.

FIGURE 12 Consumption of bulk ACh by the AChE monomer at different ionic strengths.



Nonconforming mesh



Conforming mesh

Figure 1. B. Lu, et al.

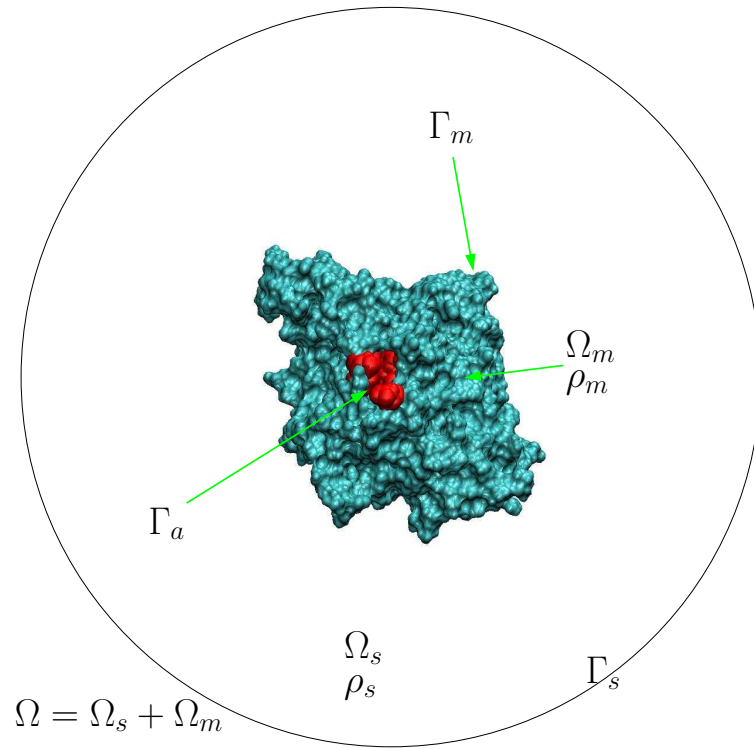
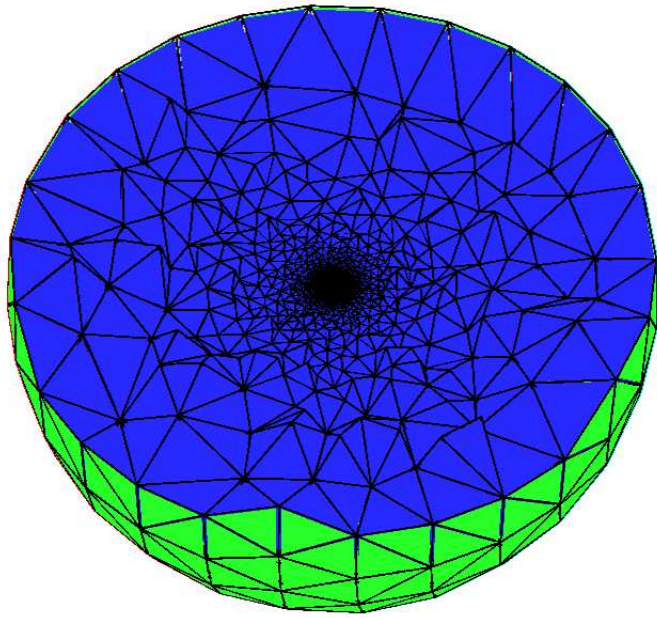
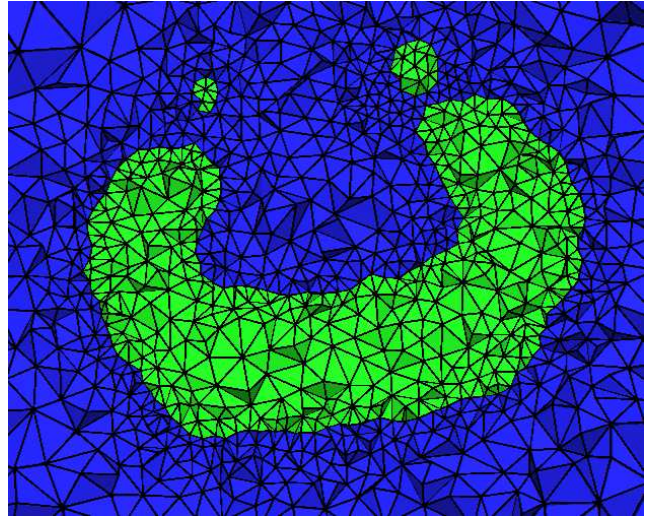


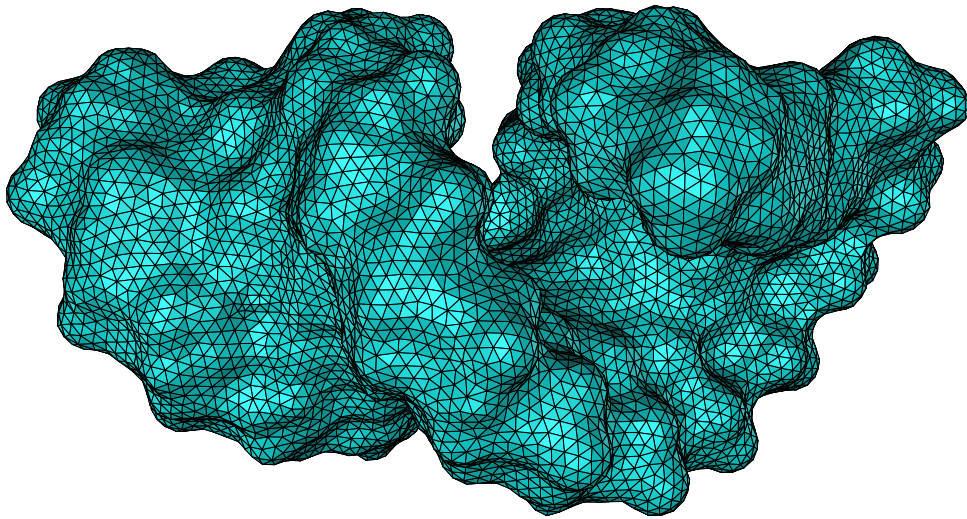
Figure 2. B. Lu, et al.



(a)



(b)



(c)

Figure 3. B. Lu, et al.

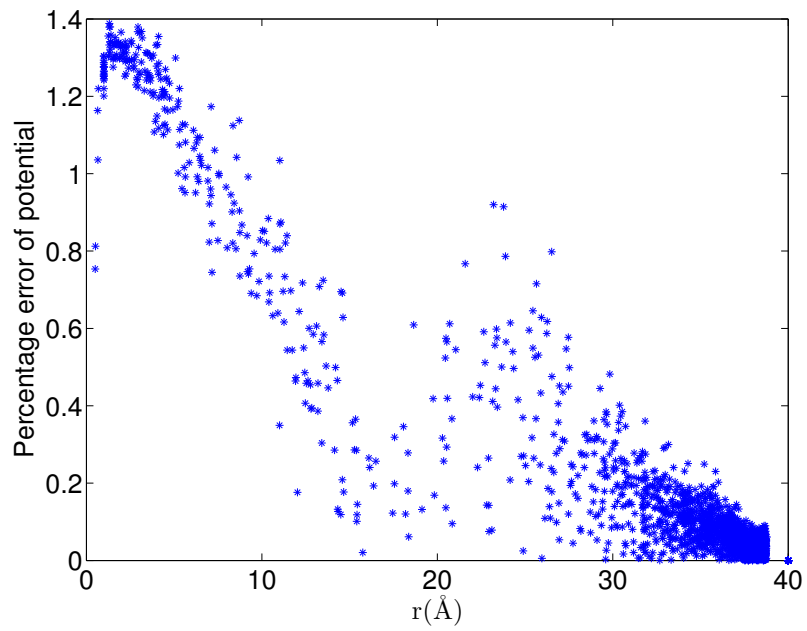
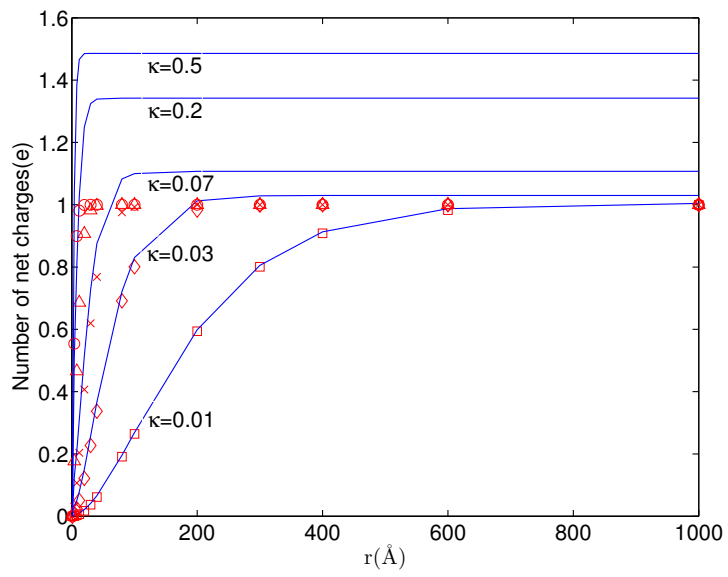
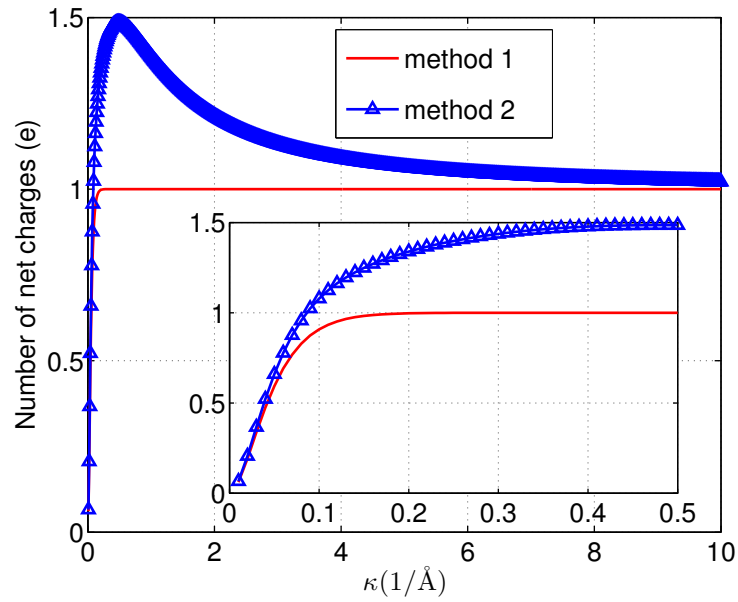


Figure 4. B. Lu, et al.



(a)



(b)

Figure 5. B. Lu, et al.

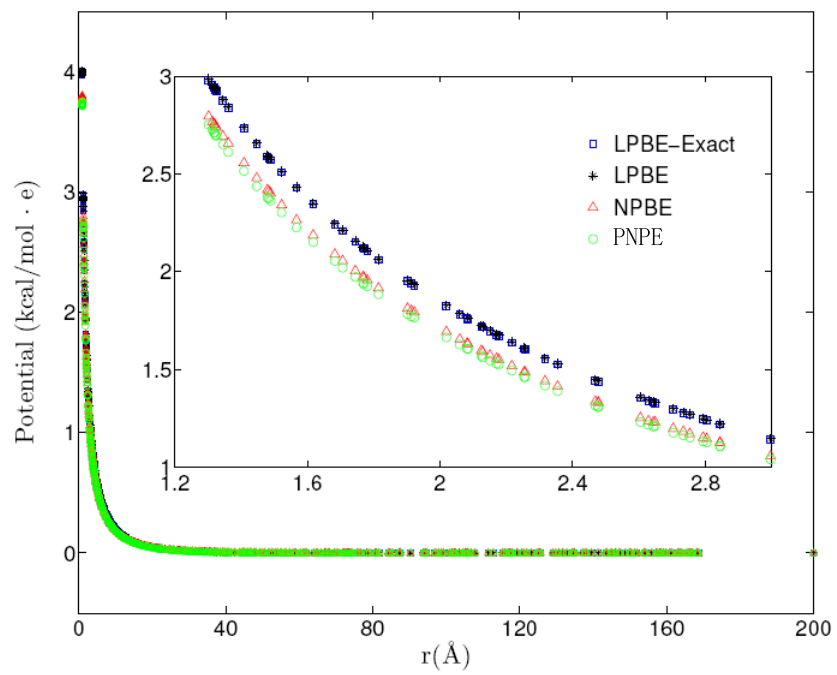


Figure 6. B. Lu, et al.

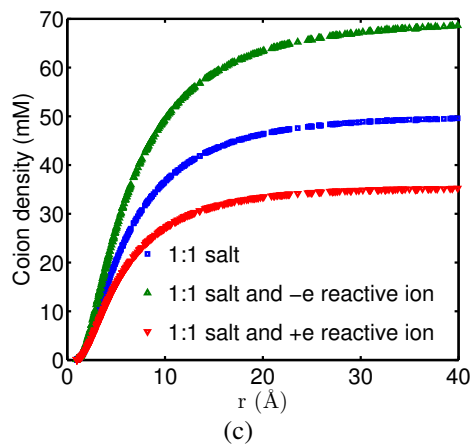
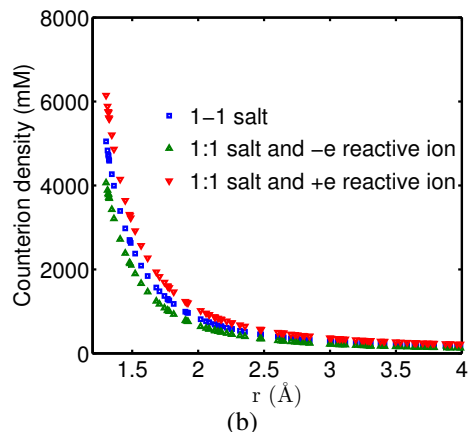
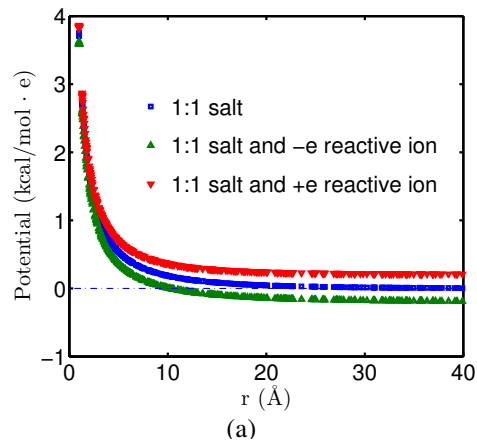
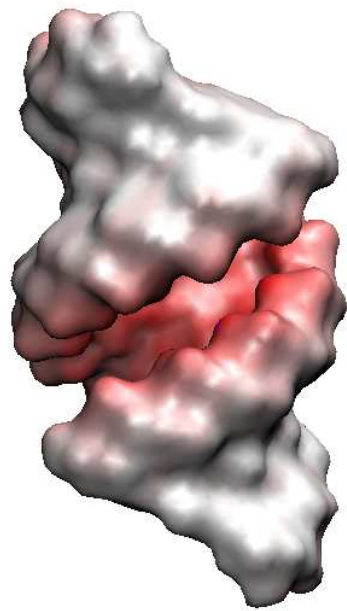
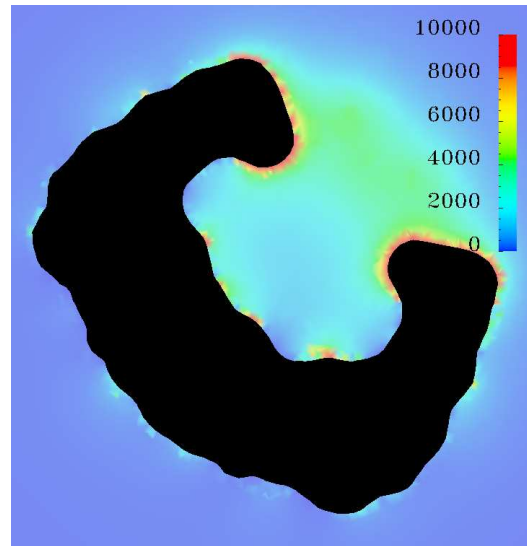


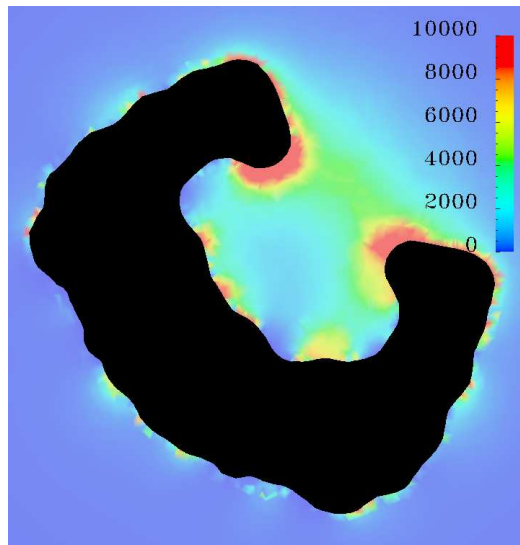
Figure 7. B. Lu, et al.



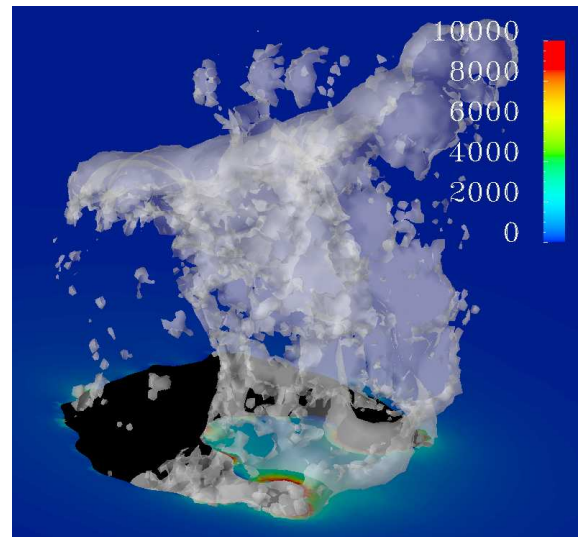
(a)



(b)



(c)



(d)

Figure 8. B. Lu, et al.

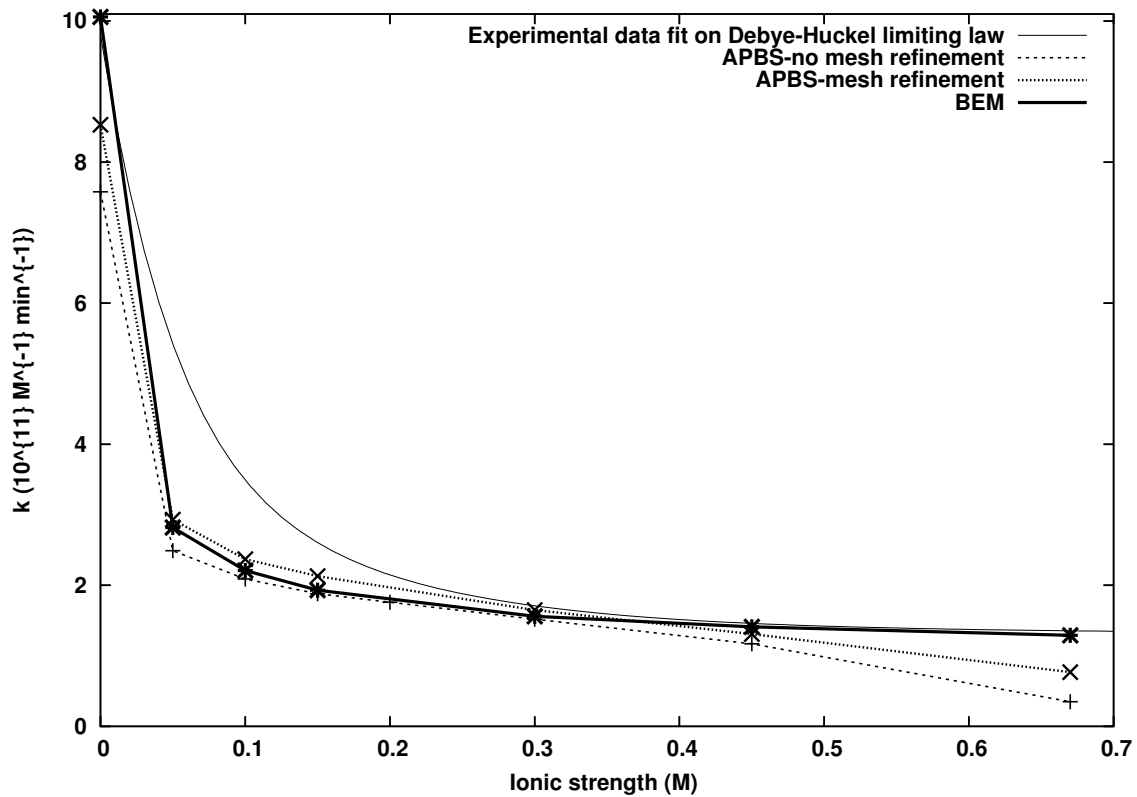


Figure 9. B. Lu, et al.

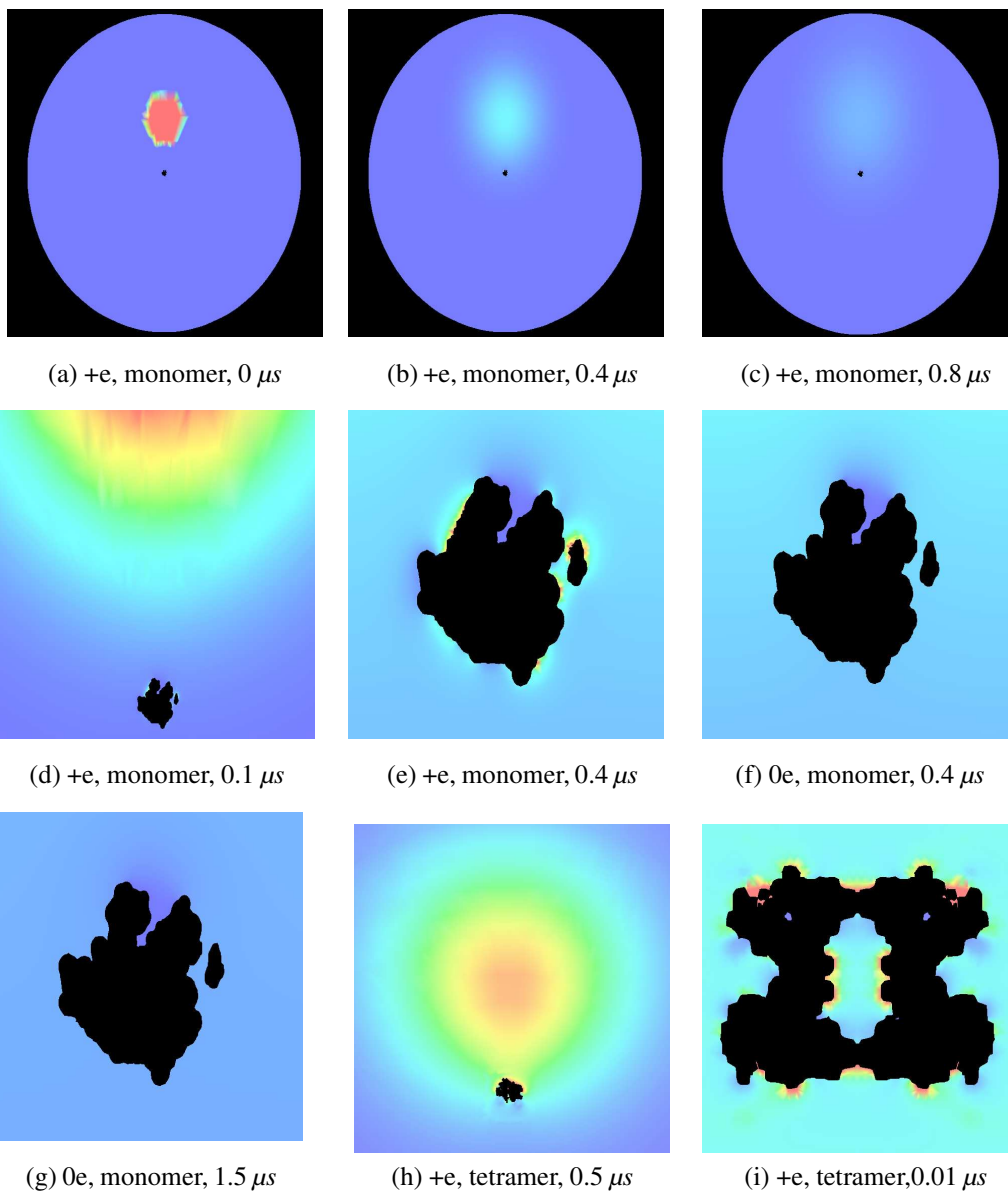


Figure 10. B. Lu, et al.

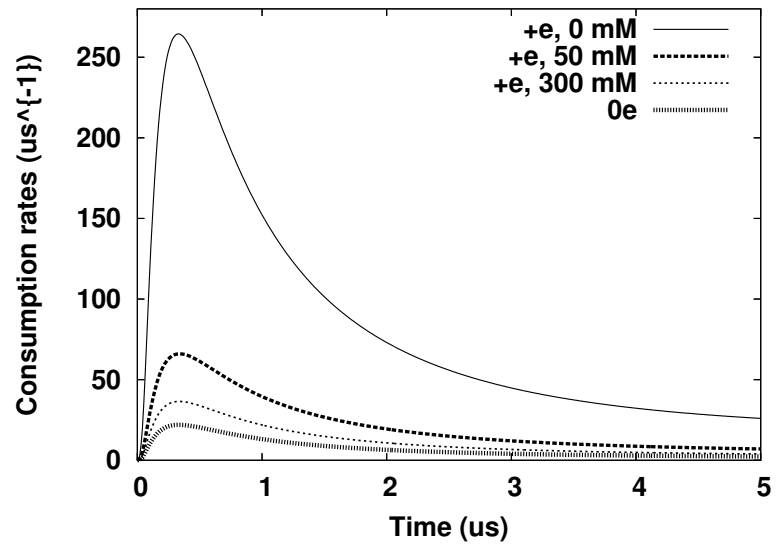
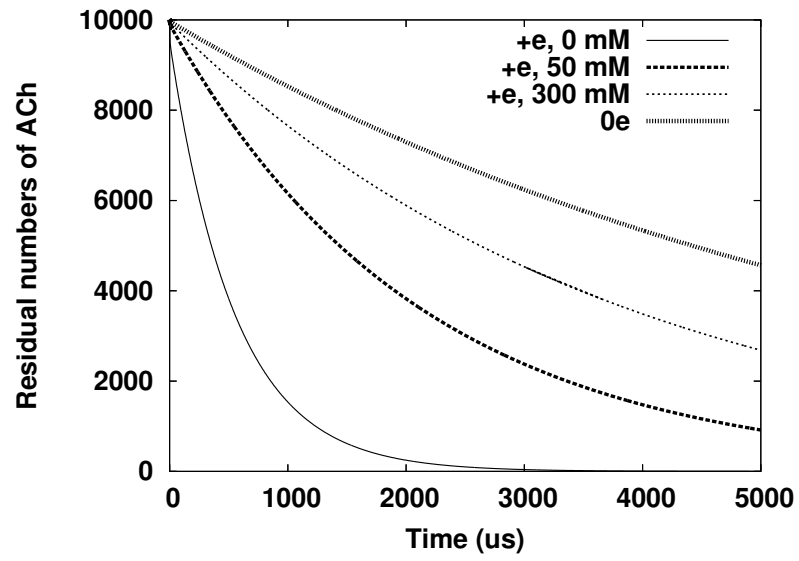


Figure 11., B. Lu, et al.

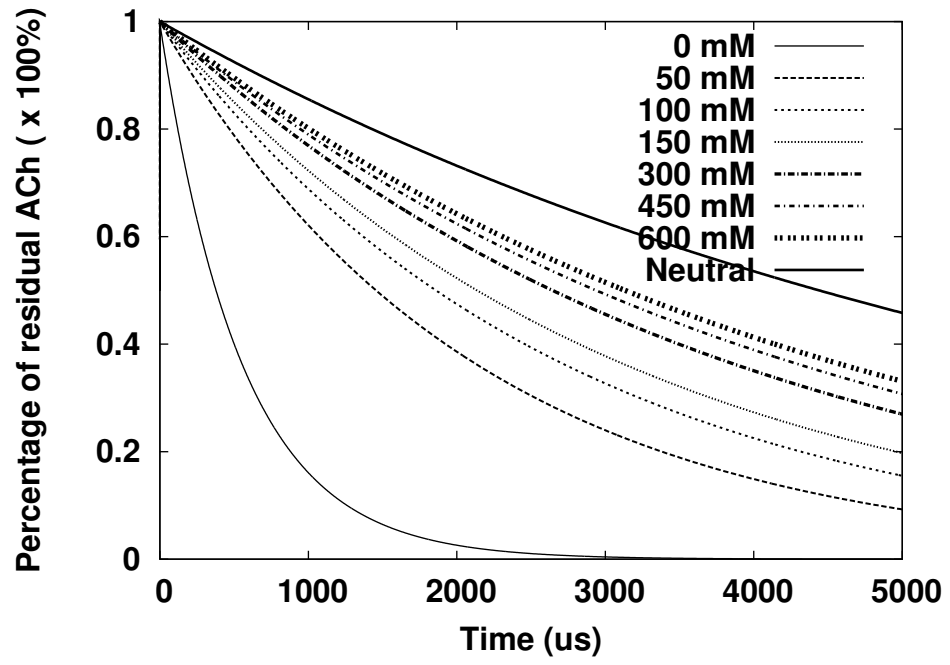


Figure 12. B. Lu, et al.